ICAS 2021 SHANGHAI
International Council of the Aeronautical Sciences
32nd Congress of the International Council of the Aeronautical Sciences
September 6-10, 2021
Pudong Shangri-La, Shanghai, China

Fluid-Structure Interaction Analysis of Elastic Effects of a Transport Aircraft Fitted with Winglets

William Martins Alves[1], Bento Silva de Mattos[1], and José Antônio Hernandes[3]

[1]Instituto Tecnológico de Aeronáutica
Aircraft Design Department
São José dos Campos, SP, Brazil
wma.mecatronica@gmail.com

[2]Instituto Tecnológico de Aeronáutica
Aircraft Design Department
São José dos Campos, SP, Brazil
bmattos@ita.br

[3]Instituto Tecnológico de Aeronáutica
Structures Department
São José dos Campos, SP, Brazil
hernandes@ita.br

Abstract

Aeroelastic effects observed in a transport airplane with winglets are computed by a fluid-structure interaction (FSI) computer simulation procedure and compared to available experimental data. The objective is the corroboration of this FSI approach to be applied to the design of morphing winglets. The effects of the winglet on the aerodynamic and elastic characteristics of the configuration are deeply investigated. The detailed aircraft wing structure model of the KC-135 aerial refueller was built by using preliminary sizing procedures based on estimated main aerodynamic loadings, flight enveloped, V-n diagram, and detailed structural layout reports. The simulation results show excellent agreement when compared with wind tunnel and flight test data.

Keywords: fluid-structure interaction; aeroelasticity, computational fluid dynamics, aircraft design

Symbology

$L^2(\Omega_t^f)$ - Lebesgue Space

n_Ω - outward unity vector from the domain Ω

u_i - displacement vector concerning cartesian coordinates x_i

v_i - velocity vector concerning cartesian coordinates x_i

$V(\Omega_t^f)^d$ - Hilbert Space

ε_{ij} - strain tensor

Γ_ϕ - diffusion coefficient

κ - thermal conductivity

μ - dynamic viscosity

σ_{ij} - stress tensor

υ - ALE the test function (function of the motion of the domain over time)

1. Introduction

The main purpose of this investigation is the validation of a technique for the design of an adaptive winglet for transport airplanes. Within this scope, the KC-135 airplane was part of this study, mainly because there is plenty of wind tunnel and flight-test data for the KC-135 airplane from NASA reports. Computational simulations were carried out and compared to wind-tunnel tests, where the model can be considered rigid, and to flight-test data, with the airplane suffering elastic effects.

Thanks to the increase of computational power and the development of computational tools, the aircraft design process is being benefited from advanced fidelity tools of greater discipline fidelity, in the sense of producing models that are useful in making more accurate predictions and better representation of the dynamics expressed in reduced models. By using higher fidelity models, engineers can produce a reduced-order model calibrated with good predictability. Examples of these models include flight mechanics aircraft model and flight control architecture model and control systems.

1.1 Fluid-Structure Interaction Models

The field of fluid-structure interaction modeling can be classified under three major branches, following the coupling strategy, we have fully coupled, loosely coupled, and closely coupled analyses.

The fully coupled approach combines structural equations of motion and fluid dynamics equations, integrating and solving numerically equations concerning time. However, such a scheme requires a construction of the matrices that, while respecting the modeling reference frames (see **Fig. 1**), produces matrices with different orders of magnitude for solids and fluids. This fact hinders the discretization of the problem, limiting the construction of the grids and being expensive from the computational point of view, usually being used in two-dimensional problems [3].

Loosely coupled approaches [4], unlike fully coupled strategy, structural dynamics and fluid dynamics are solved using separated solvers and have different computational grid topologies in which boundaries are non-coincident. This approach has an external connection between fluid and structure modules. The fluid solver, in general, has reasonable techniques to export forces to interfacing with the structure solver.

The closed approach is one of the most widely used methods in the field of Computational Aeroelasticity. Fluid models and structures are solved in different solvers. However, it has an internal connection module that exchanges information between the two models, which intercommunicate iteratively (**Fig. 3**).

The information exchanged are the surface loads, mapped on the computational fluid dynamics (CFD) surface grid and transmitted to the structural dynamics (CSD) grid, which maps the displacement field, transferring this information to the CFD [5].

In the present work, a closed approach was employed to evaluate aeroelastic response.

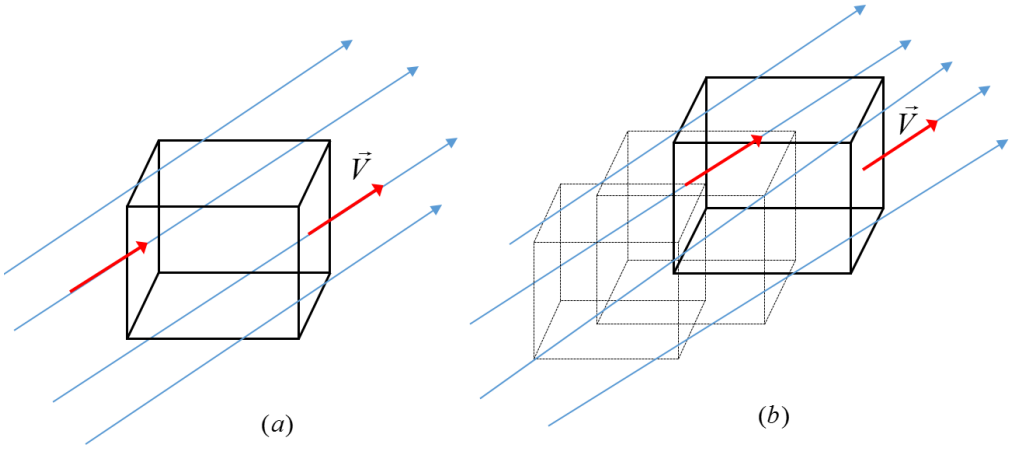

Figure 1 - Reference Frames:
(a) Eulerian control volume fixed in space.
(b) Lagrangian control volume moving and deforming with fluid flow.

1.2 Fluid Flow Dynamics Fundamental Equations

In this section, we will briefly provide an overview of the fluid dynamics equations for an Eulerian reference frame.

The fluid main behavior in this model is characterized by a linear relationship between viscous stress and strain:

$$\sigma_{ij} = \mu\left(\frac{\partial v_i}{\partial x_j} + \frac{\partial v_j}{\partial x_i} - \frac{2}{3}\frac{\partial v_k}{\partial x_k}\delta_{ij}\right) - p\delta_{ij} \tag{1}$$

The laws of conservation of mass, motion, and energy may be written as:

$$\frac{\partial \rho}{\partial t} + \frac{\partial(\rho v_i)}{\partial x_i} = 0 \tag{2}$$

$$\frac{\partial(\rho v_i)}{\partial x_i} + \frac{\partial(\rho v_i v_j)}{\partial x_j} = \frac{\partial}{\partial x_j}\left[\mu\left(\frac{\partial v_i}{\partial x_j} + \frac{\partial v_j}{\partial x_i} - \frac{2}{3}\frac{\partial v_k}{\partial x_k}\delta_{ij}\right)\right] - \frac{\partial p}{\partial x_i} + \rho f_i \tag{3}$$

$$\frac{\partial(\rho e)}{\partial t} + \frac{\partial(\rho v_i e)}{\partial x_i} = \mu\left[\frac{\partial v_i}{\partial x_j}\left(\frac{\partial v_i}{\partial x_j} + \frac{\partial v_j}{\partial x_i}\right) - \frac{2}{3}\left(\frac{\partial v_i}{\partial x_i}\right)^2\right] - p\frac{\partial v_i}{\partial x_i} + \frac{\partial}{\partial x_i}\left(\kappa\frac{\partial v_i}{\partial x_i}\right) + \rho q \tag{4}$$

where ρ is the density of the fluid, f_i are the external forces, and *q* represents heat sources.

In this work, The realizable $k-\varepsilon$ turbulence model was employed and it was considered an enhanced wall treatment in which the entire domain is subdivided into a viscous-affected near-wall region and a fully-turbulent region determined by a wall-based turbulent Reynolds number and interpolated by enhanced wall functions that approximate expected boundary layer behavior and the region between viscous-affected and fully turbulent is represented by a blending function.

To solve numerically partial differential equations of fluid flow, a finite volume method was used, which embraces approximation of integral by applying Gauss's divergence theorem.

This technique integrates the partial differential equations over each control volume to find discretized equations to each control volume, conserving physical quantities (e.g., mass, heat transfer) to each control volume.

This method is applied over a conservation equation reformulated into the general form, called as general transport equation [6], written in its differential form:

$$\frac{\partial \rho\phi}{\partial t} + div(\rho\phi u) = div(\Gamma_{\phi}\nabla\phi) + S^{\phi} \tag{5}$$

The equation (5) was written in divergence form to allows application of Gauss's theorem, that follows:

$$\frac{\partial}{\partial t}\int_{\Omega}\rho\phi d\Omega + \oint_{\Gamma} J\cdot n d\Gamma = \int_{\Omega} S^{\phi} d\Omega \tag{6}$$

Integrating the generalized transport equation over the time interval Δt and the control volume Ω and approximate concerning time for each mesh element, we have the following finite volume formulation:

$$\frac{(\rho\phi_p)^{t+\Delta t} - (\rho\phi_p)^{t}}{\Delta t}\Delta V + \sum_{f}^{N_{faces}} \rho_f V_f \phi_f \cdot A_f = \sum_{f}^{N_{faces}} \Gamma_{\phi}\nabla\phi_f \cdot A_f + S^{\phi}V \tag{7}$$

To approximating concerning space we assume that properties are constant on a given control volume at a given time in its center of gravity, varying these properties along with element through interpolation functions in which the most known are centered, upwind (first-order or second-order accuracy), and hybrid, based on Péclet number.

The solvers generally used to handle these equations are pressure-based ones (SIMPLE, SIMPLE-C, PISO, FSM) [7][8] and density-based solvers (ROE-FDS, AUSM, HLLC) [8][9][10].

In this article, the solver used is an implicit density-based with ROE-FDS scheme, with second-order upwind scheme applied in the flow and on turbulence model (calculation of kinetic energy and dissipation rates). The condition of convergence is based on the Courant number for given cell size and time step.

1.3 Structural dynamics approach

In these models, we consider the Lagrangian reference frame and a linear relationship between stress and strain.

$$\varepsilon_{ij} = \frac{1}{2}\left(\frac{\partial u_i}{\partial x_j} + \frac{\partial u_j}{\partial x_i}\right) \tag{8}$$

The equations of linear elasticity are derived from linear stress and strain relationship and describe conservation of displacement and are known as equations of motion, in its generalized form, known as Navier-Cauchy equations for linear elasticity.

$$\rho_s \frac{\partial^2 u_i}{\partial t^2} - \nabla\cdot\sigma(u) = 0 \tag{9}$$

To solve numerically **Eq. 9** is used the finite element method (FEM) that divide the solid domain Ω_s (or Ω^s) into multiple finite elements Ω_e and the calculation of the displacement field U_e is performed on each finite element from values calculated on its nodes (points that are part of finite element edges) and interpolated by polynomials.

According to that was described in the preceding paragraph, a linear equation on the element Ω_e can be obtained:

$$U(x_i,t) = N_e(x_i)U_e(t) \tag{10}$$

where $U_e(t)$ is the nodal displacements unknowns and $N_e(x_i)$ the matrix of interpolation polynomials called shape functions (based on Hermite's polynomials).

Using the Galerkin method to discretize $U(x_i,t)$, we obtain the generalized equation of motion for each finite element as follows:

$$m_e\ddot{u}_e + k_e u_e = f_e \tag{11}$$

with elementary mass matrices m_e, stiffness elementary matrix k_e, and external forces vector represented by the element f_e.

Assembling the equations of all elements presents into the domain, we have the generalized equation of motion to the domain Ω_s:

$$[M]\{\ddot{u}\} + [C]\{\dot{u}\} + [K]\{u\} = [F(t)] \tag{12}$$

The equation can be solved using a modal approach in which the solution is composed by eigenvectors of the vibration subproblem, which can be written as n individual equations, corresponding one equation to each vibration shape mode, as follows:

$$\begin{cases} \ddot{u}_i(t) + 2\xi_i\omega_i\ddot{u}_i(t) + \omega_i^2 u_i(t) = f_i(t) & i = 1,2,3,\ldots,n \\ f_i(t) = \Phi_i^T[F(t)] \end{cases} \tag{13}$$

where ω_i is the natural frequency for *i*th mode and ξ_i is the damping parameter for *i*th mode.

To solve this system is necessary to calculate numerically integrals in the mass and stiffness matrices using Gaussian quadrature and after that, solve the linear system to obtain displacement vector through Gauss-Seidel based-methods and perform modal extraction through Lanczos Method.

1.4 The interface of Fluid Flow and Structures

In the case of the FSI problem we consider a solid domain Ω^s and a fluid domain Ω^f in contact with each other along with the interface $\Gamma_{f/s}$ (as we can see in **Fig. 2**)

We have that the density of contact forces on the fluid in the solid domain perspective written as:

$$t_s = \sigma_s n_s \tag{14}$$

And similarly, the density of contact forces on the fluid in the fluid domain perspective written as:

$$t_f = \sigma_f n_f \tag{15}$$

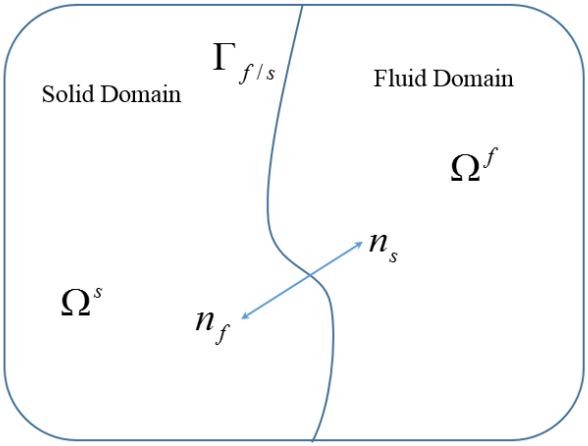

Figure 2 - FSI domains.

To solid domain, we have the Dirichlet displacement function u and Dirichlet data functions based on velocity vector v on boundary conditions. Therefore, two assumptions are made to solve this general problem.

The first assumption is that the velocities are continuous along with the interface $\Gamma_{f/s}$, given by:

$$v = \dot{u} \tag{16}$$

The other assumption is relative to the mechanical equilibrium on $\Gamma_{f/s}$

$$t_s + t_f = 0 \tag{17}$$

The normal vectors are linked by the following relationship:

$$n = n_s = -n_f \tag{18}$$

Therefore, the interface equilibrium condition arises:

$$\left(\sigma_f - \sigma_s\right) n = 0 \tag{19}$$

To model meshing motion in the fluid domain is necessary to reconcile characteristics of both reference frames seen in **Fig. 1**, to allow carry through a control volume quantity of mass and heat, and at the same time, this control volume may deform and move with time.

To meet these requirements, there is an Arbitrary Lagrangian-Eulerian (ALE) formulation that combines the regions in the fluid domain where we need to approximate a Lagrangian formulation to follow particle motion (for example close to the interface between the fluid and the solid domains) and the regions where an Eulerian description is sufficient to describe the flow (far away from solid domain).

This formulation is succinctly described by **Eq. 21**.

$$\begin{cases} \text{Find } (v, p) \in V(\Omega_t^f)^d \times L^2(\Omega_t^f), t \in I \text{ such that} \\ \int\limits_{\Omega_t^f} \left[\left.\frac{\partial v}{\partial t}\right|_x + (v - w)\cdot\nabla v \right] \upsilon d\Omega = \int\limits_{\Omega_t^f} \left[p\nabla\cdot\upsilon - \frac{2}{\mathrm{Re}}\nabla v : d(\upsilon) + b_f \cdot \upsilon \right] d\Omega, \ \forall \upsilon \in V(\Omega_t^f)^d \\ \int\limits_{\Omega_t^f} (\nabla\cdot v) q d\Omega = 0, \ \forall q \in L^2(\Omega_t^f) \end{cases} \tag{20}$$

Applying the Galerkin Method, substituting velocity and pressure fields by its discretized versions and the original spaces by approximation spaces and its respective test functions, we have:

$$\begin{cases} \text{Find } (v_h, p_h) \in M_H \times P_H \text{ such that} \\ \sum_{i=1}^{2K} v_i \int_{\Omega_t^f} q_l \nabla \cdot \upsilon_i d\Omega = 0 \\ \sum_{i=1}^{2K} \frac{\partial v_i}{\partial t} \int_{\Omega_t^f} \upsilon_k \cdot \upsilon_i d\Omega + \sum_{i=1}^{2K} v_i \int_{\Omega_t^f} \upsilon_k \cdot (v - w) \cdot \nabla \upsilon_i d\Omega = \\ \sum_{j=1}^{2K} p_j \int_{\Omega_t^f} q_l \nabla \cdot \upsilon_k d\Omega - \frac{1}{\mathrm{Re}} \sum_{i=1}^{2K} v_i \int_{\Omega_t^f} \nabla \upsilon_k : (\nabla \upsilon_i + [\nabla \upsilon_k]^T) d\Omega \\ \forall (\upsilon_k, q_l)_{k=1\ldots 2K; l=1\ldots L} \in M_H \times P_H \end{cases} \quad (21)$$

The spatial discretization of this model is realized by choosing special types of elements, Crouzeix–Raviart that allows a discontinuous approximation of the pressure or Taylor-Hood elements which allows continuous approximation of the pressure. The temporal discretization has the following form:

$$\begin{cases} \nabla \cdot v^{n+1} = 0 \\ \left(\frac{3v^{n+1} - 4v^n + v^{n+1}}{2\Delta t} \right) + \left(v^* - w \right) \cdot \nabla v^* = -\nabla p^{n+1} + \frac{1}{\mathrm{Re}} \nabla v^* \end{cases} \quad (22)$$

with

$$\nabla p^{n+1} = \frac{3}{2\Delta t} \nabla \cdot v^* - \nabla p^n \quad (23)$$

To determine the velocity field, we must deal with nonlinearities present on the convective term within ALE. This limitation is resolved using the iterative fixed-point method or Picard's method to minimize residues as assures the ALE algorithm convergence.

The position of mesh motion is determined using the spring analogy, suggested by Hartwich and Agrawal [18], in which the strategy was based on the master/slave node relationship between the moving surface points (masterpoints) and vertices located at the other blocks (slave points).

The movement of the masterpoints is based on the displacements obtained from the structural calculation solver. The movement of the slave points depends on the movement of its corresponding master point from point x_m to x_{m+1} and slave points move from x_s to x_{s+1}.

$$x_{s+1} = x_s + \theta (x_{m+1} - x_m) \quad (24)$$

where θ is a decay function that depends on stiffness factor β, in which larger values mean that meshes acts like a rigid body and $f_{\min}$ ensures optimal remeshing behavior if master nodes present small displacements.

$$\theta = \exp\left\{ -\beta \min\left[\left(f_{\min}, \frac{dv}{(\varsigma + dm)} \right) \right] \right\} \quad (25)$$

where dv and dm are spatial gradients and a ς number sufficient small to avoid division by zero.

$$dv = \sqrt{(x_v - x_m)^2 + (y_v - y_m)^2 + (z_v - z_m)^2}$$
$$dm = \sqrt{(x_{m+1} - x_m)^2 + (y_{m+1} - y_m)^2 + (z_{m+1} - z_m)^2} \quad (26)$$

Fig. 3 summarizes fluid-structure Interaction numerical calculation. CFD and CSD (FEM) solvers perform calculations normally in regions where the domain is purely solid or fluid.

In the fluid-structure interface region, the ALE solver performs the fluid computation by emulating a lagrangian fluid particle frame, sending and interpolating in the solid mesh of the interface region the virtual displacements resulting from the velocity field and the forces from the pressure field (see **Fig. 4**).

The FEM solver calculates the deformations and the equilibrium condition of the interface is checked by the coupling module. If this condition is not attained, the coupling module sends the deformations calculated by the FEM solver to the dynamic mesher of the fluid domain, which deforms the mesh and the calculations restart and the iterations continue until the equilibrium condition is reached.

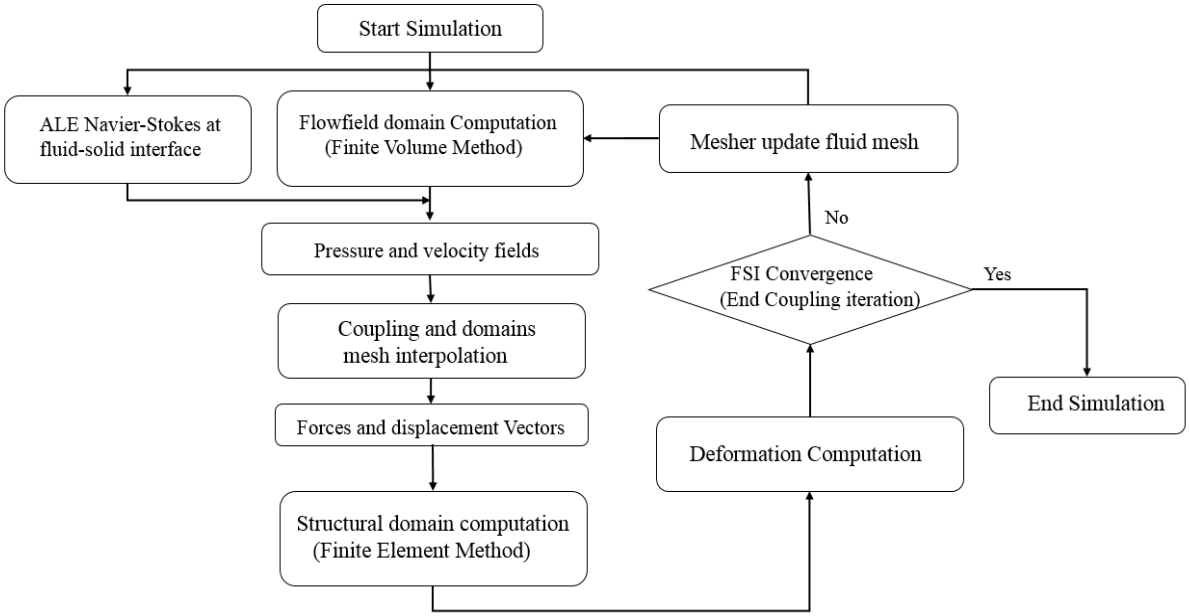

Figure 3 - Fluid-structure coupling procedure.

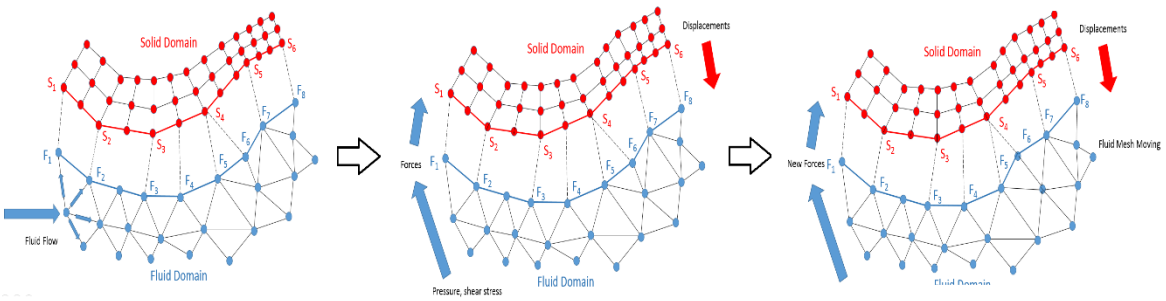

Figure 4 - Mesh domains coupling and interpolation.

2. Modeling the KC-135 transport airplane

In this section, the procedure for the construction of the model for winglet effect analysis will be described. The aircraft that will be used in the analysis is the Boeing KC 135 aerial tanker (**Fig. 5**), whose results from the tests [19] will be used to validate the model, to make some predictions about the behavior regarding the presence of winglets.

The next step refers to preprocessing. Based on the data from the Almojuela [20] (**Figs. 6-7**) article and reference [24]. The detailed structural layout can be recovered as well as its flight envelope (**Fig. 8**) and V-n diagram (**Fig. 10**). The geometry of the KC135 model could then be constructed by using CAD software, as can be seen in **Fig. 11**.

Fig. 9 shows the structural calculation process for the wing used in the analysis, where based on the performance data of the aircraft, we have the design loads that are reflected in load distributions along the wingspan and along the chord. Even considering that design loads consider maneuver, gust loads, rolling acceleration, flap loading, ailerons loading, the weight of fuel tanks, systems, and engines, we need to keep in mind that it is necessary to ensure design margins to withstand unforeseen loads and adverse operational conditions.

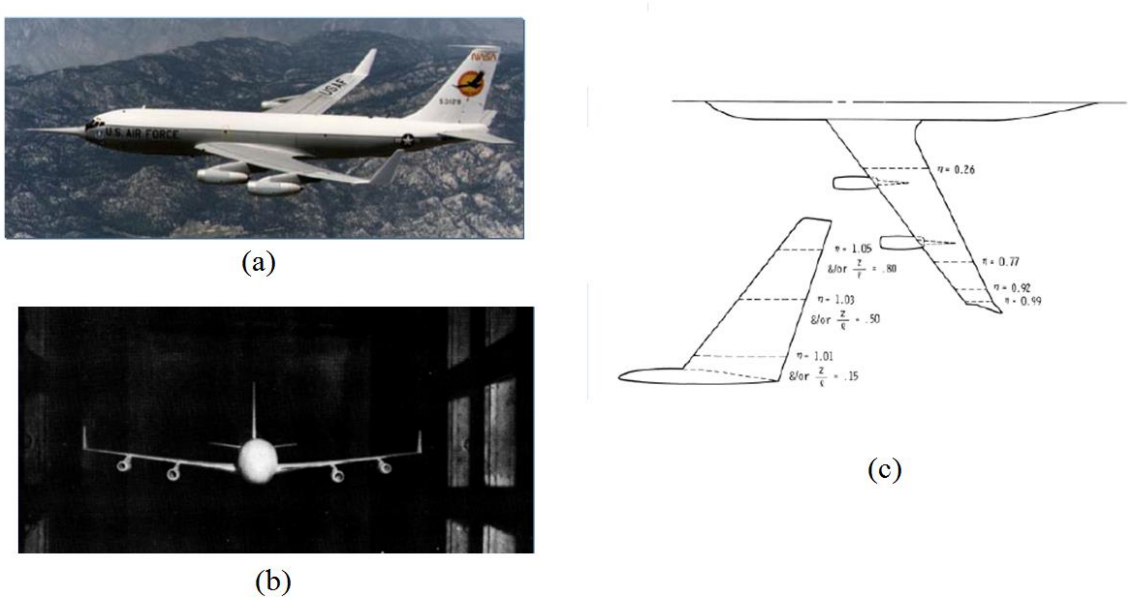

Figure 5 - Boeing KC 135 Stratotanker (adapted from [19]):
(a) KC 135 flight test.
(b) KC 135 wind tunnel testing.
(c) Wing and winglet static pressure orifice locations.

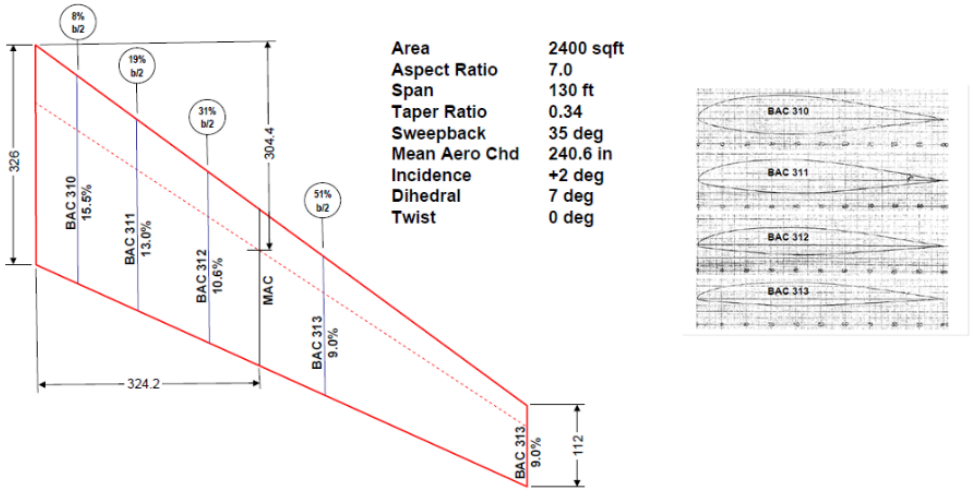

Figure 6 - Wing Design data: Planform and airfoils (adapted from [20]).

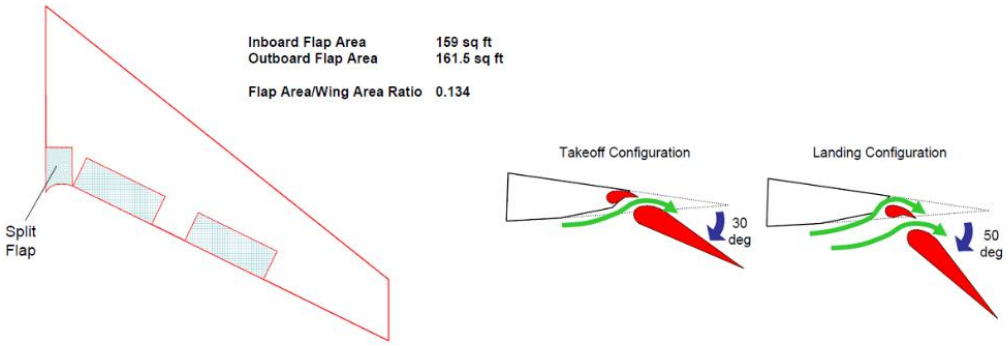

Figure 7 - Flap dimensions and operational data (adapted from [20]).

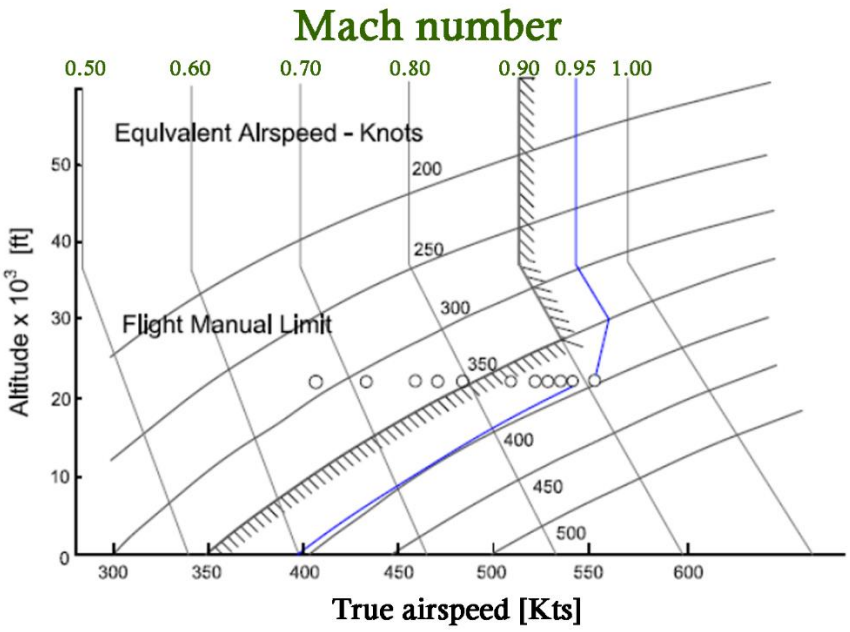

Figure 8 - Boeing KC 135 Stratotanker flight envelope (adapted from [19]):

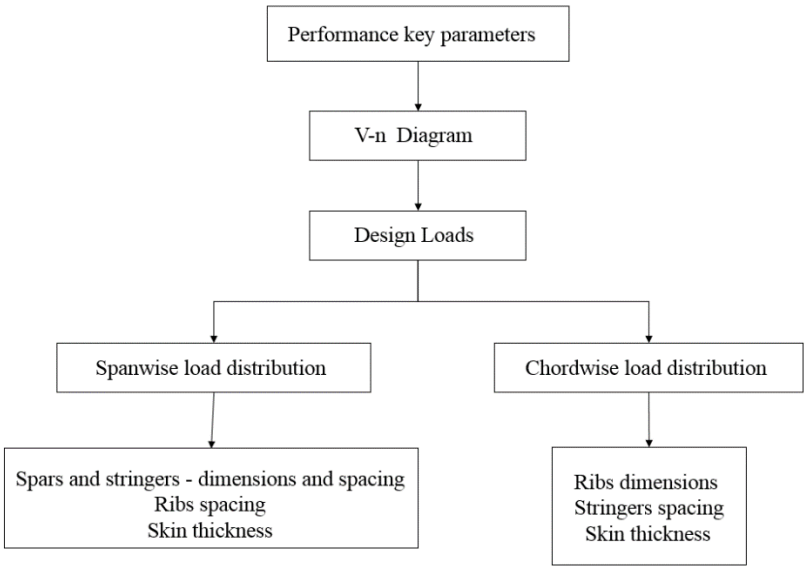

Figure 9 – Wingbox structural elements calculation process.

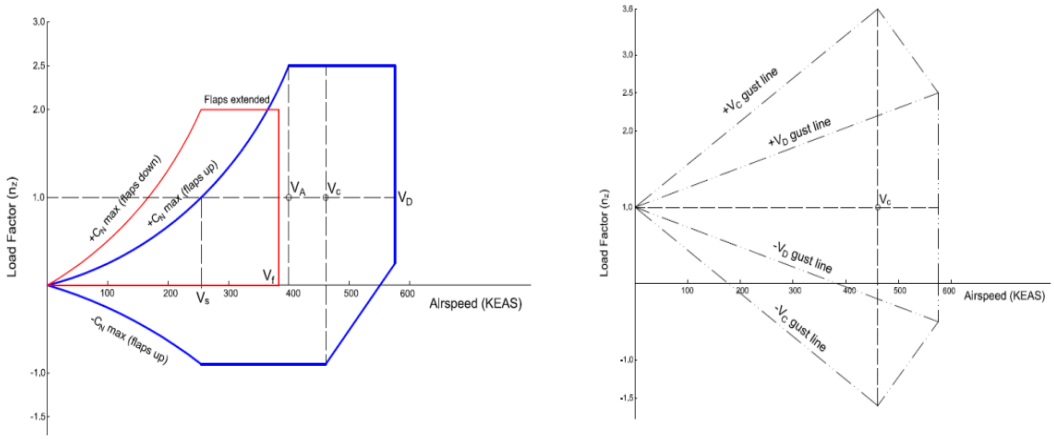

Figure 10 - Maneuver and Gust V-n Diagram for KC 135.

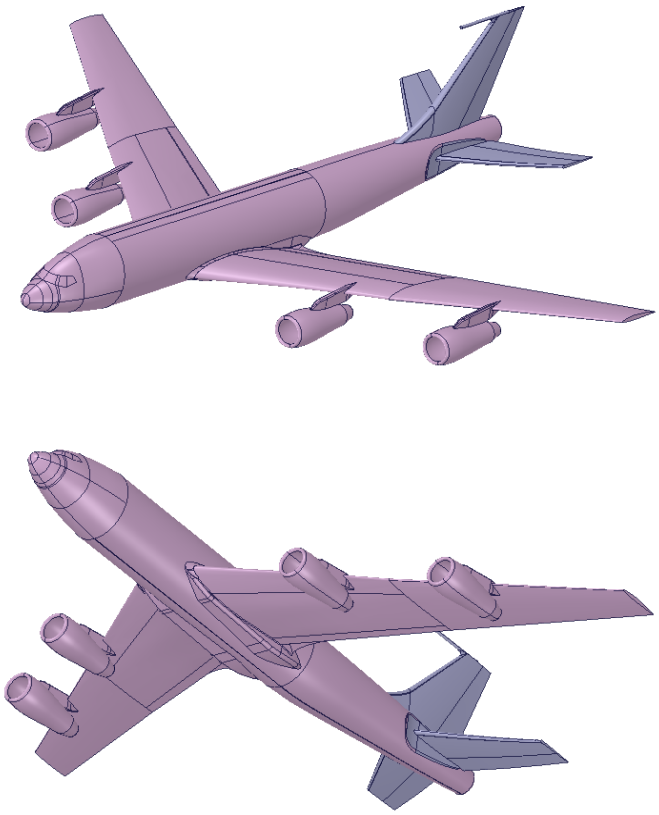

Figure 11 – CAD model of the KC 135 military tanker.

Schrenk approximation (**Fig. 12**) is used to determine the overall span-wise lift distribution. The method states that the resultant load distribution is an arithmetic mean of an elliptical distribution of the same span and area and a load distribution representing the actual planform shape. This method is used in preliminary stages to wing, without considering control and high lift surfaces.

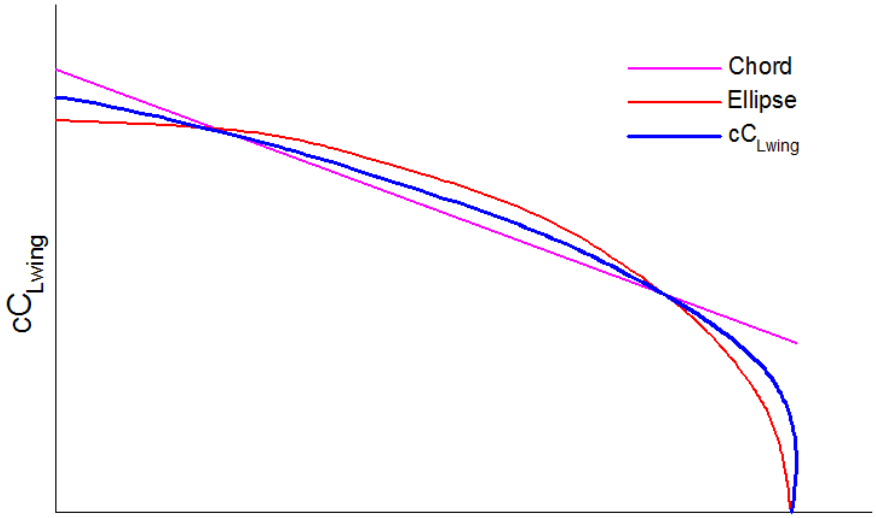

Figure 12 – Example of Schrenk Approximation.

To deal with this limitation, the method was adapted by the author and consists of taking the boundaries of the Schrenk method to mean secant line as points of new elliptical distribution, further enhancing the calculations previously made to accommodate loads from flaps, ailerons, rolling acceleration, etc.

The premise is based on the original approach which is based on relationships between the elliptical wing area and the area of an actual wing, being the percentage of surface area proportional to the chord at that station concerning the wing and consequently proportional to the intensity of the variation of the lift component in that wing station.

Once using the modified method illustrated in **Fig. 13**, we apply it to the case of the airplane with typical loadings of the structure, fuel, and systems based on its typical spanwise density. A pre-analysis based on CFD and calculations of more realistic components showed that the premise of the adapted method is reasonable, as we can see in **Fig. 14**.

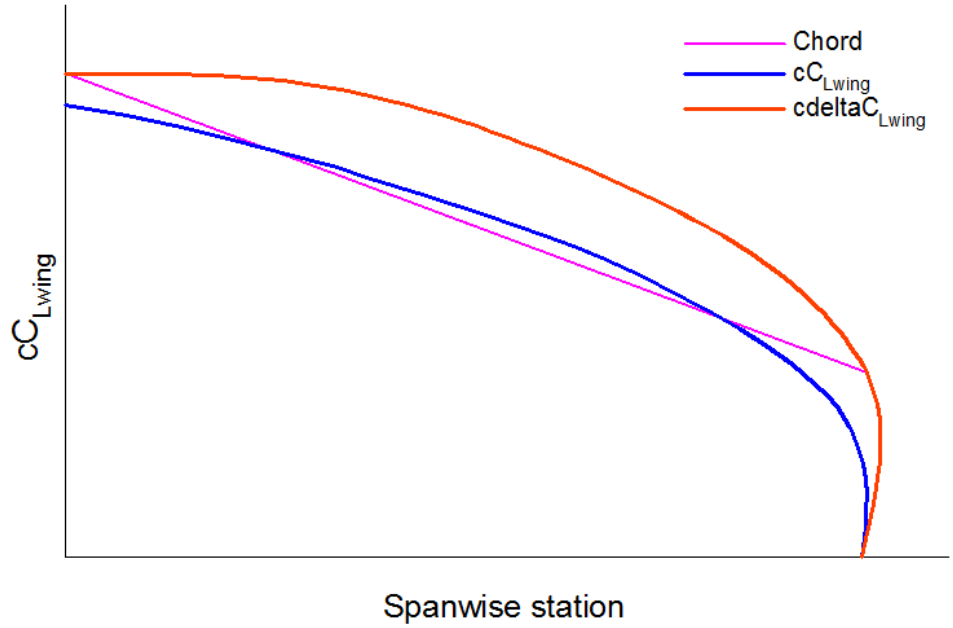

Figure 13 – Example spanwise wing loading calculated by the modified Schrenk approximation.

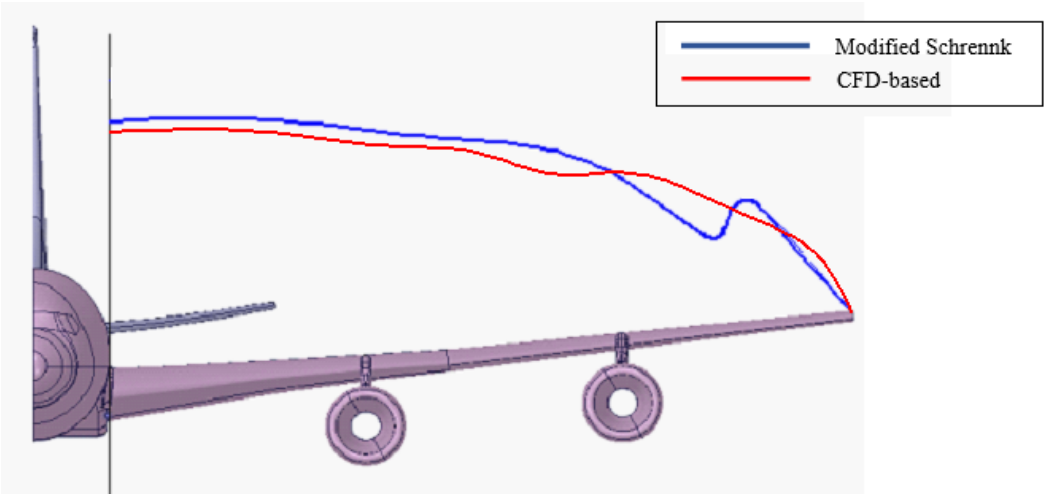

Figure 14 – Preliminary resultant spanwise loads Schrenk modified approximation of KC 135 wing and comparison with spanwise load obtained based on CFD calculations.

The spanwise distribution was important for dimensioning the components whose buckling and shear stresses are significant, such as stringers and spars sections and the addition of moment of inertia by the number of stringers and spacing of both stringers and spars.

The chordwise distributions were important for dimensioning the local buckling of the stringers and the shearing stresses under the ribs.

The thickness of the skin is influenced by the spanwise and chordwise loadings that affect the panel buckling of each wing station. An example of such distributions can be seen in **Fig. 15**.

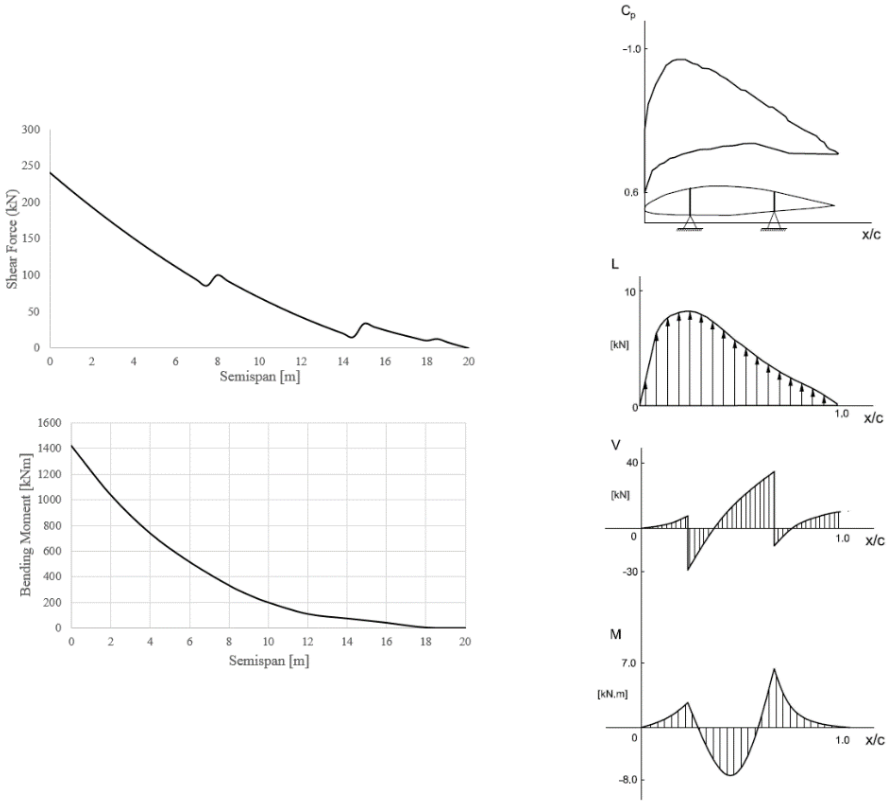

(a) **(b)**

Fig. 15 – Representation of load diagrams:
(a) Shear Force and Bending Moment along semispan
(b) Typical Pressure Coefficient, lift chordwise distribution, shear diagram, moment diagram, and shear flow across wing section (26% of half span).

From these diagrams, the wing elements, summarized in Table 1, whose dimensions were obtained from [22], [23], and [24], are measured, noting that the wing is like the real wing.

Table 1 - Wing structural elements calculated vs data.

	Calculated	Data
Skin average thickness [in]	0.05	0.038
Ribs minimum thickness range [in]	0.025-0.098	-
Ribs maximum allowable spacing [in]	32.48	26.4-28.5
Stringers maximum allowable spacing [in]	13.39	12.5
Spars chord relative position [%]	23.5/65	23/65
Spars average thickness [in]	0.285	0.32
Semispan structural weight MTOW fraction [%]	10.19	10.41

In **Fig. 16**, we can see the simplified structural layout of the KC-135 wingbox.

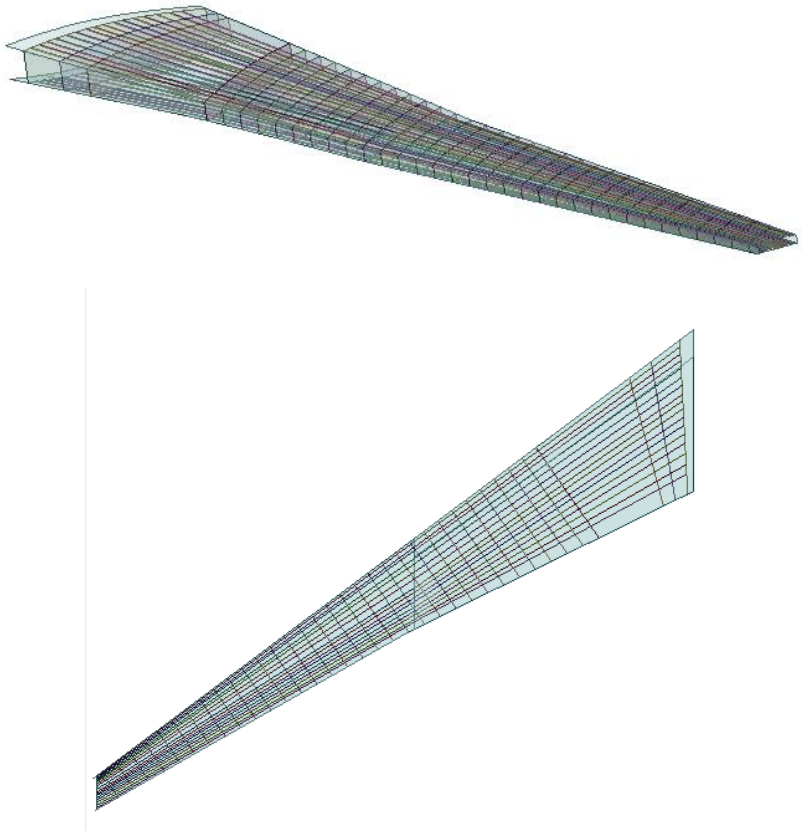

Figure 16 - Boeing KC 135 Wingbox (Structure layout) CAD simplified model for simulation purposes.

To verify if the reconstitution of the wing design is feasible, an stress analysis was carried out, as can be seen in figure 17 where it is verified that the structural wing used in the simulations has a design margin.

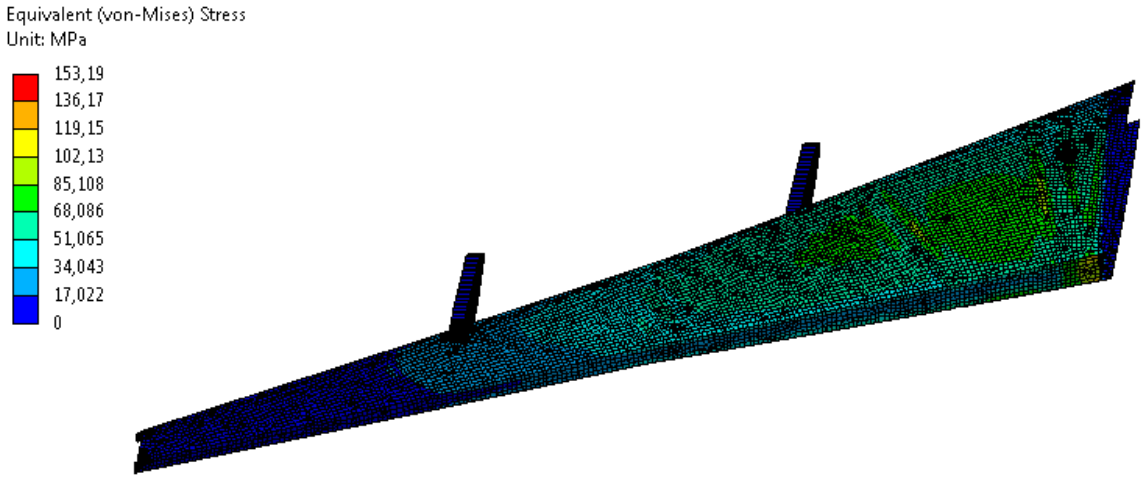

Figure 17 - Resulting KC 135 preliminary wing stress analysis.

After the creation of the geometrical model, the computational meshes are built. The finite element meshes were constructed with quadrilateral shell elements to meet the skewness criteria of elements as close as possible to 0, which guarantees the accuracy of the analyzes (**Fig. 18**).

In the case of the Structural model, the meshes referring to the geometry of the outer surfaces of the wing were defined as the fluid-structure interaction interfaces as well as the communication parameters with the Multiphysics coupling module, discretized in quadrilaterals shell elements with skewness values between 0.22-0.26.

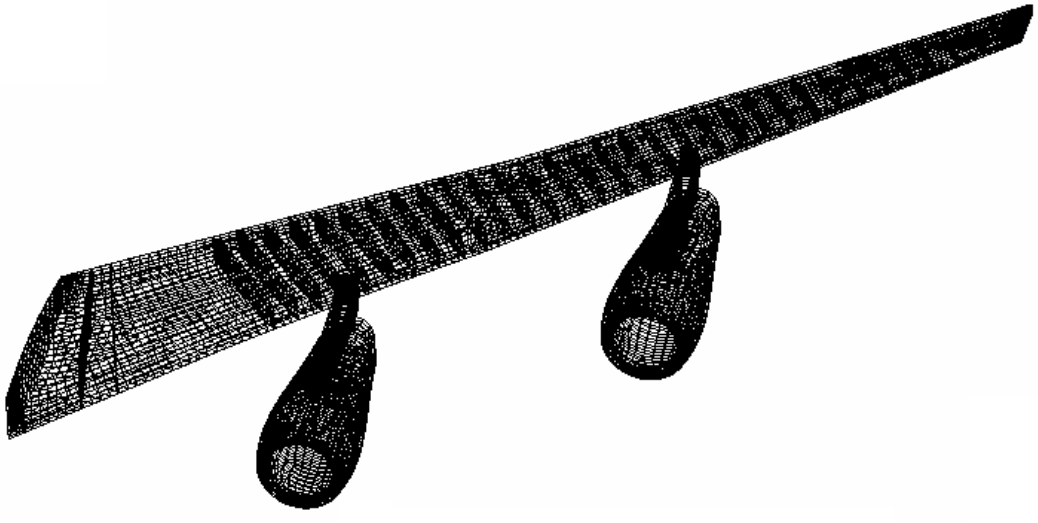

Figure 18 - Wing Computational Pre-processing CSD Mesh.

CFD meshes (**Fig. 19**) were constructed using tetrahedral and hexahedral elements to meet the orthogonal quality criteria of cells close as possible to 1, to ensure the convergence and the use of inflation close to the walls, to allow the accurate calculation of the boundary layer in the region through interpolation of the wall functions. The mesh of the fluid model was discretized in tetrahedral elements with orthogonal mesh metrics values between 0.85-0.92.

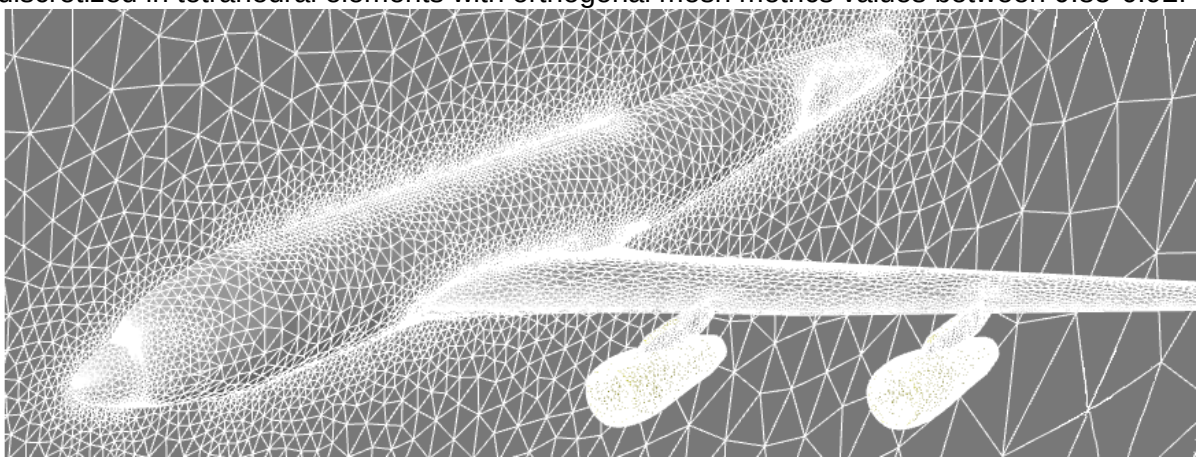

Figure 19 – CFD mesh for KC-135 airplane.

In the step concerning model set up, after defining the atmospheric properties of interest and boundary conditions, the CFD model of the analyzes has as characteristics the air properties being modeled as a perfect gas, considering hydrodynamic and thermal boundary layers, using a realizable $k-\varepsilon$ turbulence model and an implicit ROE-FDS solver with full multigrid initialization (FMG) and dynamic mesh with remeshing smoothing behavior to interact through FSI coupling with the structural solver.

To perform the simulations described later in the next section, the geometry of the winglet had its values of dihedral (cant angle) modified to verify these effects on winglet performance. In this work, simulations were performed with the complete aircraft and for simplicity and better visualization, the results are shown for the clean wing without the engines, except in mode shape results.

3. Results

In this section, we will present simulation results, regarding validation of the model and some predictions will be done.

In **Fig. 20**, streamlines are displayed and a vorticity pattern can be seen in **Fig. 21**. These vortices, while present, represent the increase of the induced drag and it can be verified that a wing with a winglet has reduces the strength of tip vortices, which means a reduction of induced drag. The local understating of this phenomenon can be verified by a lower gradient of the wing loading at the tip (the local gradient is related to the trailing-vortex strength).

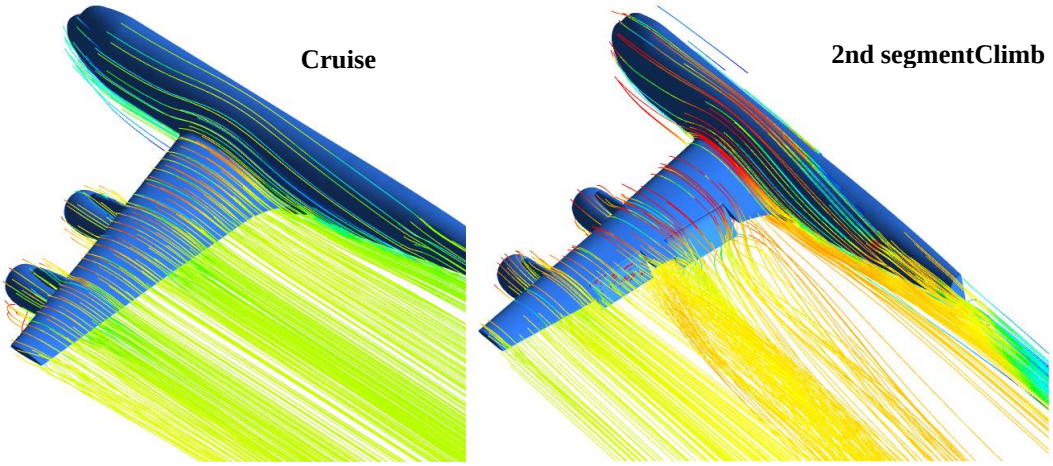

Figure 20 - Complete Aircraft CFD Analysis without winglet (cruise and climb segments).

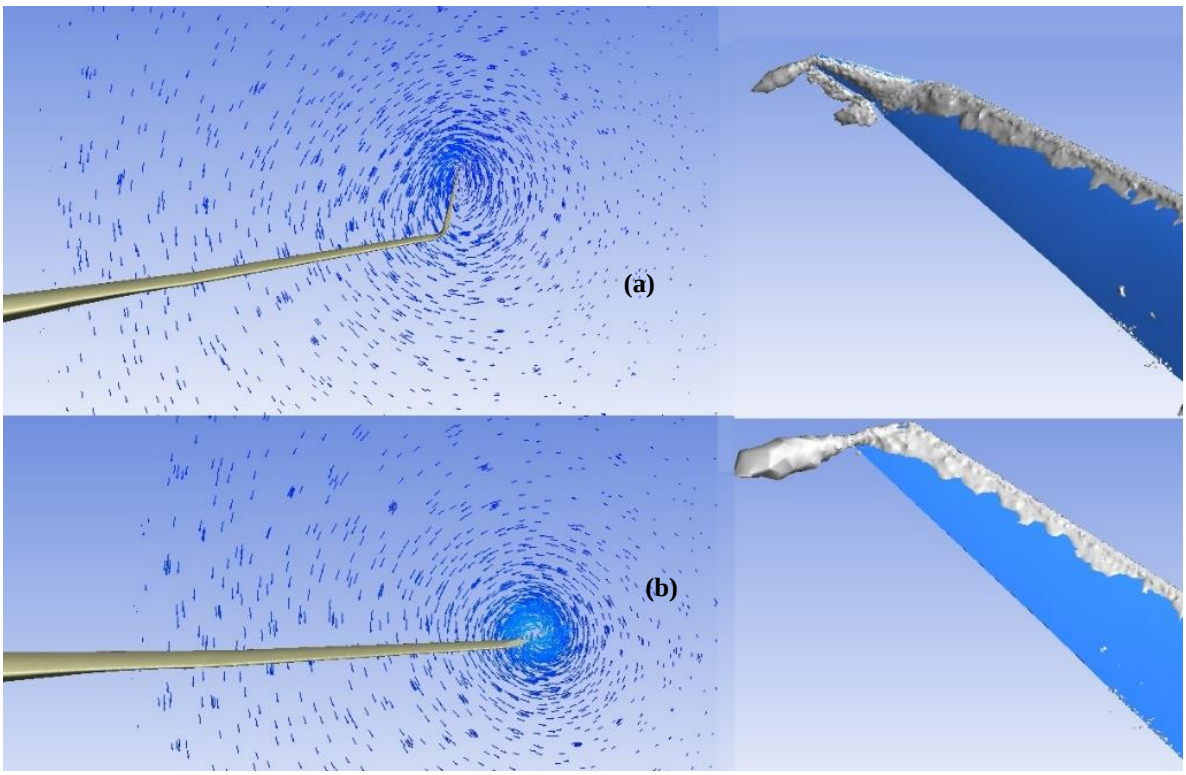

Figure 21 - CFD Wing Analysis – Vorticity pattern:
(a)With winglet 15º/-4º.
(a) Not winglet.

In Figs. **22 to 24**, the comparison of Cp distributions between the calculated one and that from the flight and wind-tunnel tests It can be noted that the presence of the winglet causes the unloading to the root section and increases the loading at the wingtip due to the decrease of the Cp and also making the distribution of Cp a little more to the trailing edge of the wing profiles.

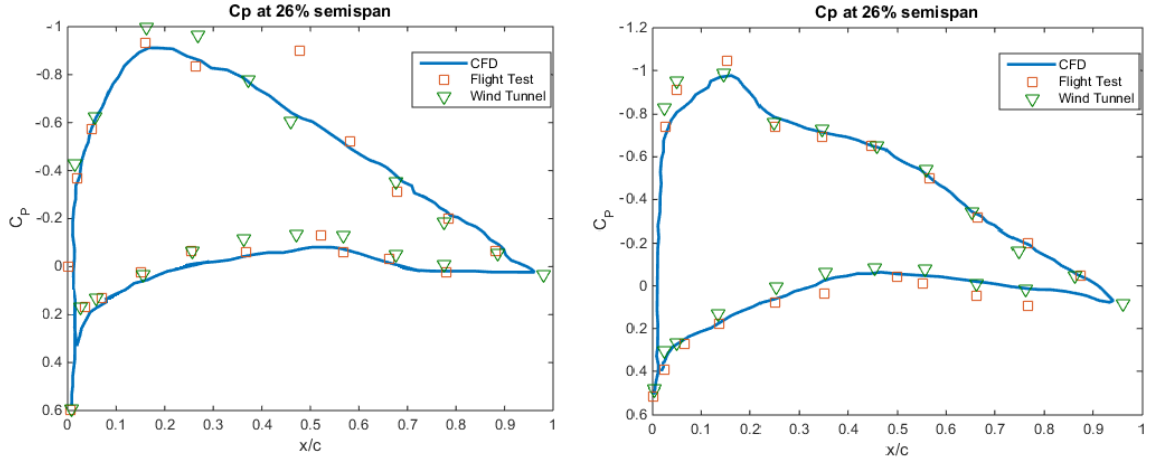

(b) **(b)**

Figure 22 - Model Validation at 26% of semispan(h=0.26) – M=0.70, α=3.5º:
(a) Baseline wing.
(b) Wing fitted with winglets 15º/-4º.

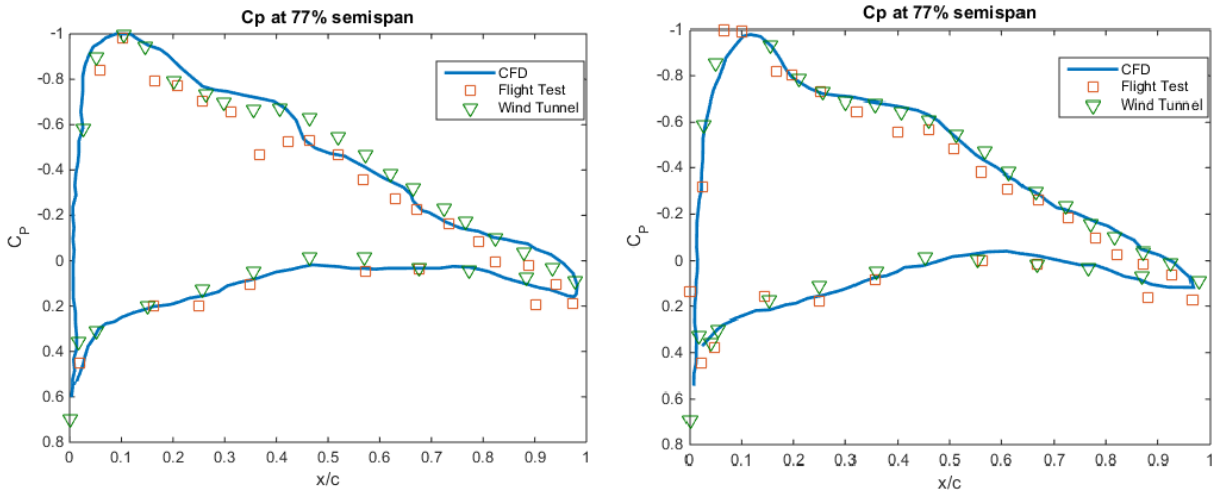

(a) **(b)**

Figure 23 - Model Validation at 77% of semispan(h=0.77) – M=0.70, α=3.5º:
(a) Baseline wing.
(b) Wing with winglet 15º/-4º.

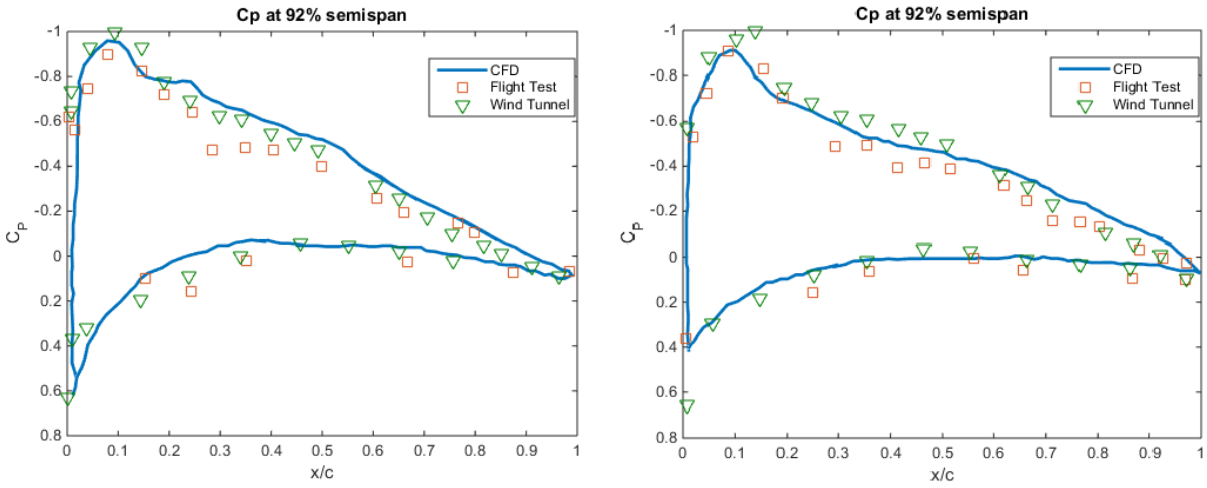

Figure 24 - Model Validation at 92% of semispan (h=0.92) – M=0.70, α=3.5º:
(a) Baseline wing.
(b) Wing with winglet 15º/-4º.

Figs 25 and 26, the effect of elasticity of the structure due to aerodynamic loads can be easily perceived. **Figs. 25-26(a),** the model is considered undeformed, with results being very similar to that from the wind-tunnel test, which is considered to be rigid; In **Figure 25-26(b),** we have the same effects of the actual wing, which is flexible.

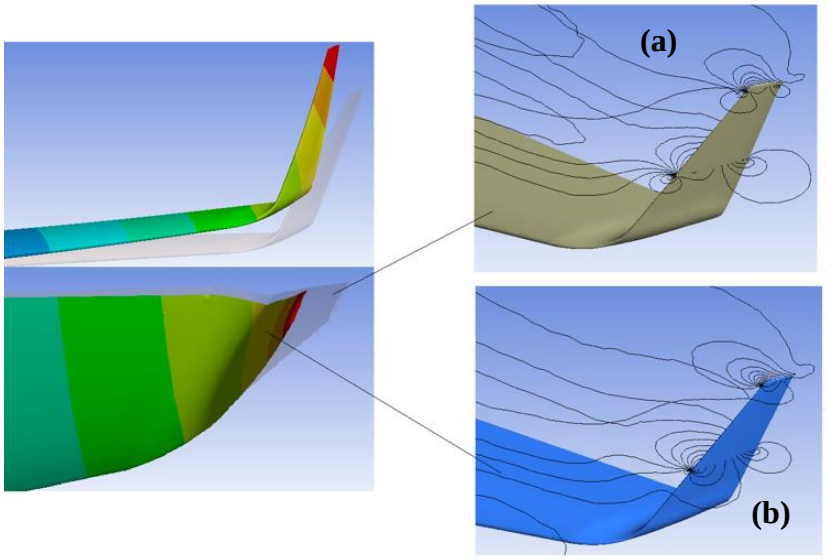

Figure 25. Effect of flexibility on pressure field– M=0.70, α=3.5º:
(a) Wing with winglet 15º/-4º undeformed (only CFD).
(b) Wing with winglet 15º/-4º with deformation (FSI).

Fig. 26 illustrates this fact occurring in the central profile of the winglet, with the pressure fields reducing their suction range in the winglet extrados.

In **Fig. 28**, the effect of the winglet dihedral variation can be observed. For the same lift coefficient as the wing without winglet, the winglet unloads aerodynamically the root of the wing, carrying more and more the tip as this angle of dihedral increases.

This effect can be intensified, as can be seen in **Fig. 27**, where the increase of the local lift coefficient (integration of the Cp distribution on the surface) can be verified as the twist angle of the winglet increases.

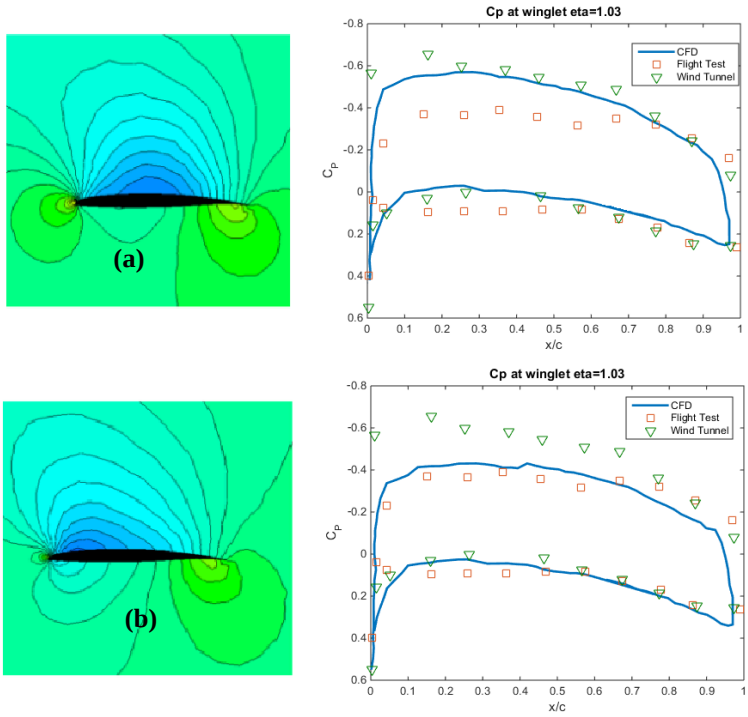

Figure 26 - Effect of flexibility on pressure field (at h=1.03):
(a) Wing with winglet 15º/-4º undeformed (only CFD).
(b) Wing with winglet 15º/-4º with deformation (FSI).

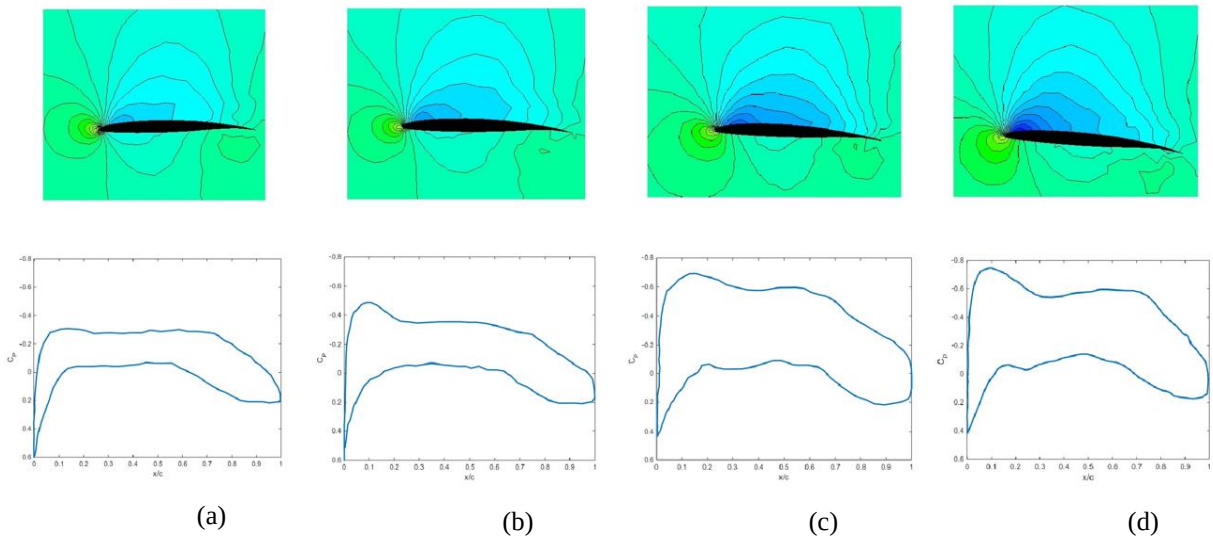

(a) (b) (c) (d)

Figure 27 - Effect of twist variation on pressure coefficient at winglet tip – M=0.70, α=3.5º.
(a) 0º (b) -2º (c) -4º (d) -6º

In figure 29, beyond model validation, we have a span load magnitude example that we observed in figure 28.

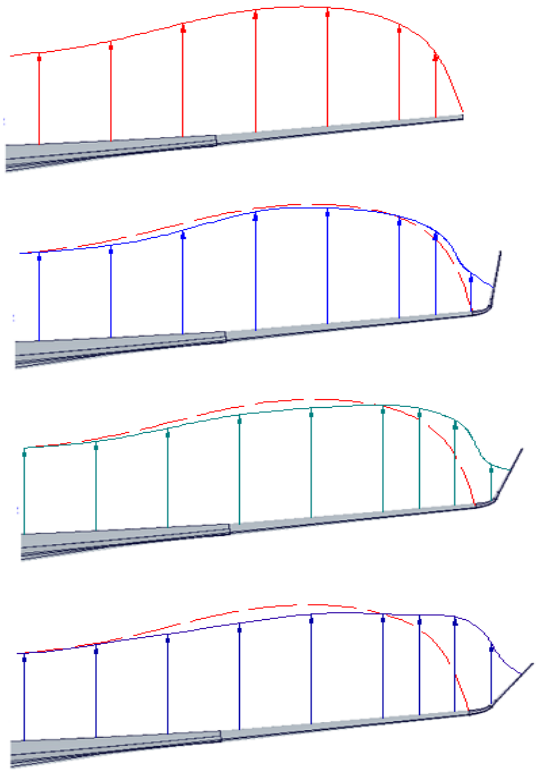

Figure 28 - Schematic effect of dihedral variation on lift distribution– M=0.70, α=3.5º.
(a) Wing baseline without winglet.
(b) Wing with winglet with dihedral 15º.
(c)- Wing with winglet with dihedral 30º.
(d) Wing with winglet with dihedral 45º.

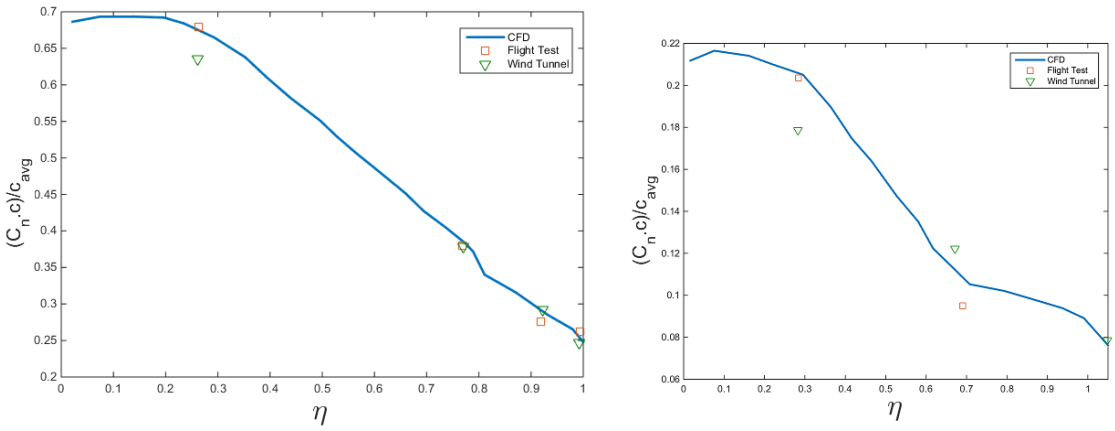

(a) (b)

Figure 29. Wing and winglet span load.
(a) Wingspan load
(b) Winglet span load

In **Figs. 30** and **31**, we verified the isolated effect of the dihedral and twist variations of the winglet on drag polar.

Both effects have the benefit of eliminating the influence of tip vortices on the rest of the wing. However, the twist variation can make the vortices less intense as the twist increases, better distributing the tip vortex along the trailing edge of the winglet. As the twist increases, the benefit decay decreases due to the parasitic drag.

The effect of the winglet dihedral variation tends to produce variations in the equivalent aspect ratio, which increases to an optimum value and then begins to decay, due to the increase of the parasite drag and induced drag as the wing with winglet approaches a normal wing.

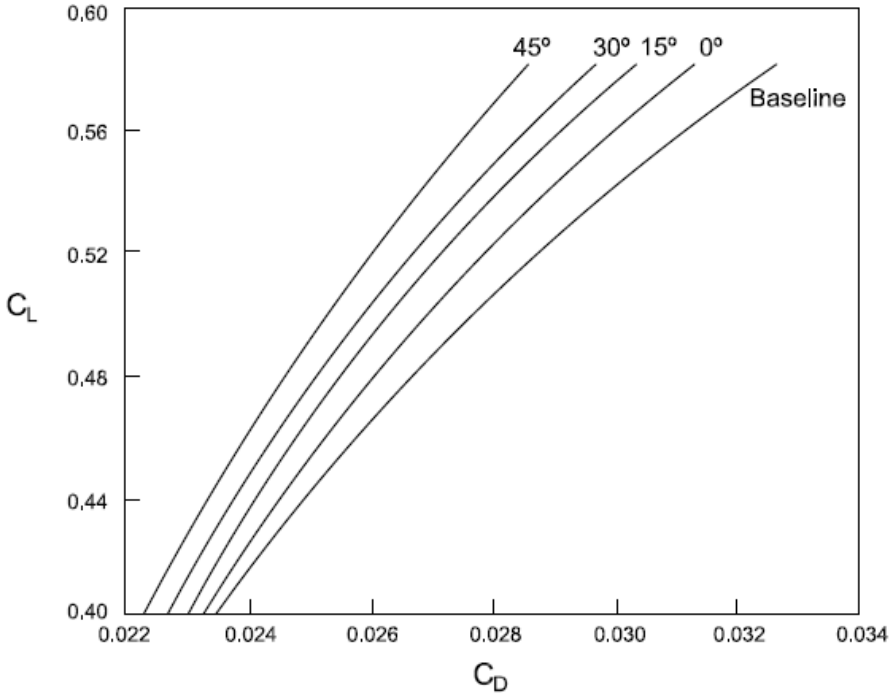

Figure 30 - Winglet dihedral angle variation on drag polar – winglet without tip twist.

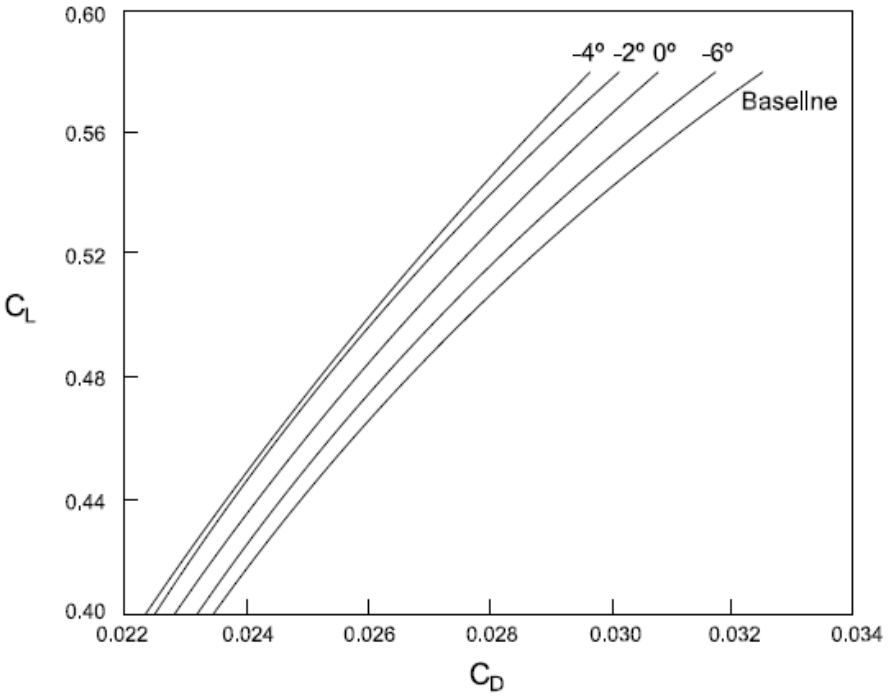

Figure 31. Winglet twist angle variation on drag polar –winglet dihedral angle of 15º.

Note that there is a relationship between dihedral angle increase and drag rise and twist angle increase (in absolute values) and drag decrease, except for the configuration with twist angle -6º.

It can be noticed that the aforementioned effects can bring mean drag reduction in cruise between 6.25% with one of the isolated effects acting and 8.91% with the combination of both effects.

In this estimation, it was taken into account measures of structural design against the phenomenon of transonic dip. According to **Fig. 30** and **31**, greater percentage reductions in drag can be achieved as the lift coefficient increases, which indicates that the climbing phase can be greatly benefited.

In **Fig. 32**, we observe the displacements in the wingtips of the wing with baseline configuration and the wing with winglet, whose wing with winglet presents greater displacement of its wingtip. The results for this point of the flight envelope are summarized in **Fig. 33**.

In **Fig. 34** it can observe the winglet effect in reducing mode shape frequencies due to mass added to wingtip. The addition of weight on the wingtip behind the elastic line increases inertia in the region and turns the wing more prone to flutter. The additional lift generated on the wingtip increases wing structural loads, consequently, increasing the bending moment at the wing root. There is an extended aerodynamic effect due to the winglet presence on the configuration. Comparing the lift distribution to the wing without winglets, the unloading of the central and inner part of the wing may further reduce the drag coefficient at transonic conditions due to the eventual reduction of the strength of shock waves there.

Considering that the climb phase would be greatly affected by the reduction of induced drag, as has been stated, one factor which greatly diminishes this benefit is the increase of inertia of the wing caused by the winglet, affecting flutter velocity, whose values tend to decrease.

In **Fig. 35**, we have summarized the results of bending moment for the design point, in which there is a relation between the decrease of the twist angle and the increase of the bending moment, except for the configuration with twist angle -6º.

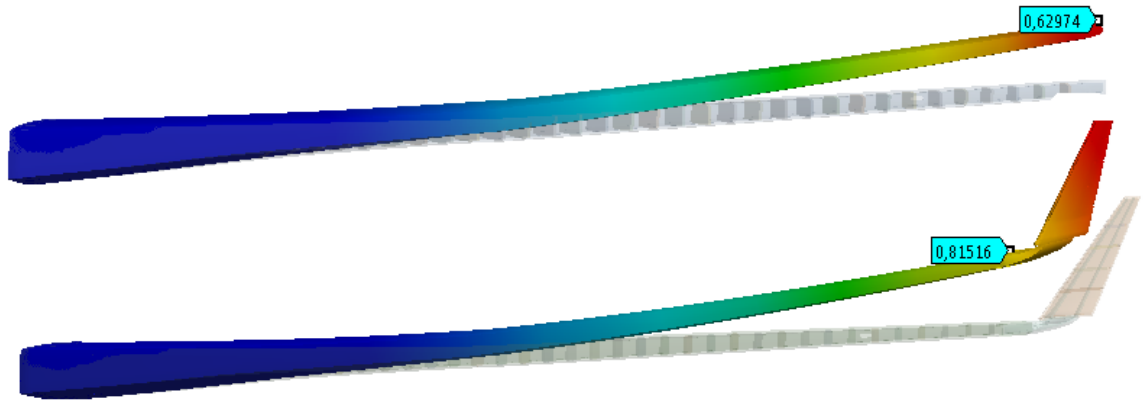

Figure 32 - Wing baseline tip displacement (in meters) – M=0.70, α=3.5º.

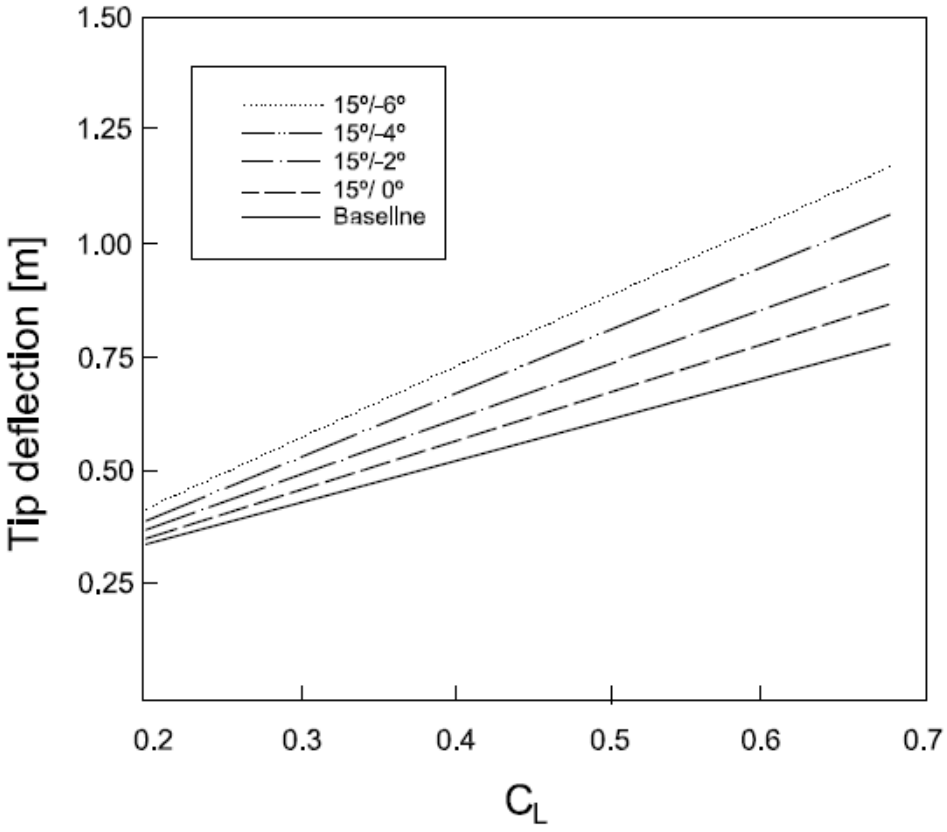

Figure 33 - Wingtip deflection (in meters) - M=0.70, α=3.5º.

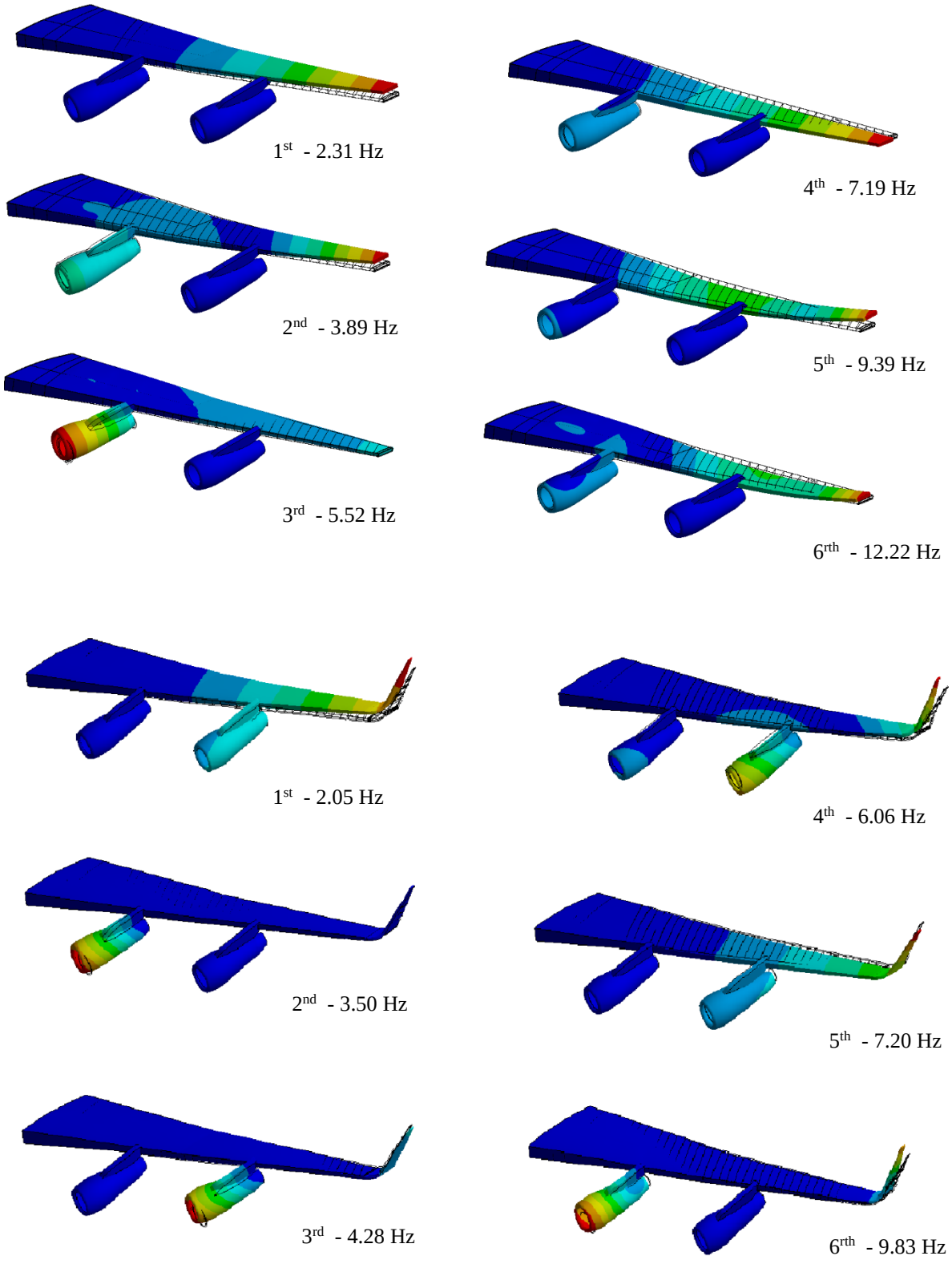

Figure 34 - Mode shapes and frequencies of baseline wing with and without winglets.

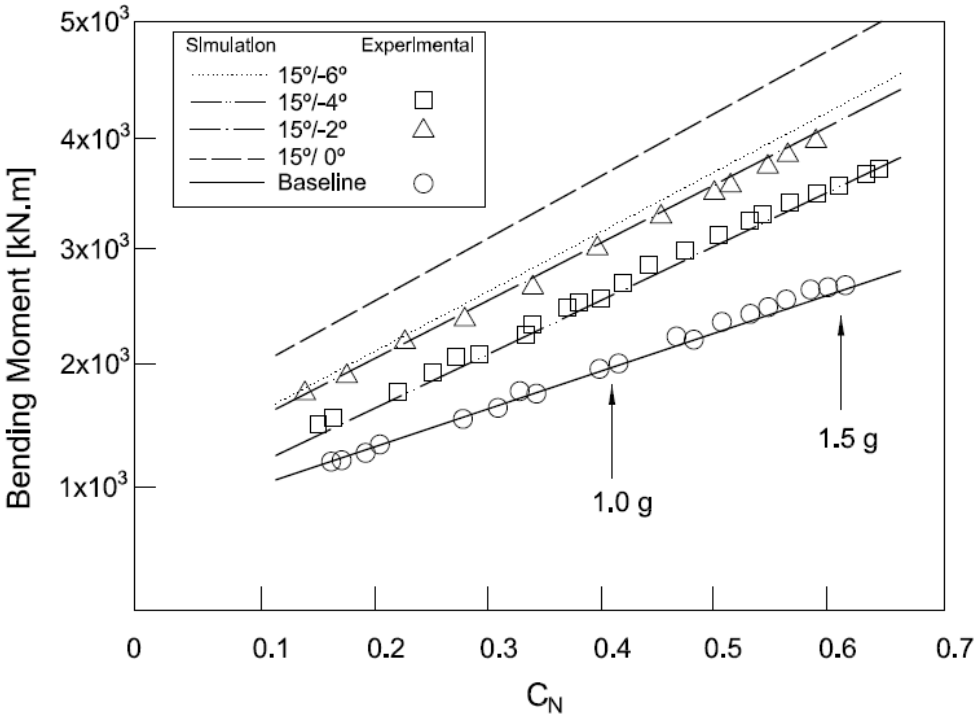

Figure 35 - Bending Moment - M=0.78, α=2.5º

In **Table 2**, we can verify the effects of the dihedral angle of the winglet, so that we can notice by the variations of the stability derivatives values, in which increasing effective wing dihedral we have the stabilizing effect that the winglets confer to the lateral dynamics, negatively affecting Dutch Roll damping. The winglet effect on increasing side force derivatives can also affect the crosswind capability of the aircraft.

Table 2 - Stability Derivatives – Reference values at M=0.77 [21].

Winglet Dihedral Angle (degrees)		0	15	30	45
Stability Derivative	Reference values	Negative Increase (%)			
$C_{Y\beta}$ [deg^{-1}]	-0.0133	15.20	14.31	12.16	6.08
$C_{l\beta}$ [deg^{-1}]	-0.0035	29.10	29.36	29.52	29.60
C_{lp} [rad^{-1}]	-0.345	13.10	13.18	13.24	13.32
C_{nr} [rad^{-1}]	-0.194	8.20	7.61	4.89	3.24
$C_{m\alpha}$ [deg^{-1}]	-0.015	31.58	31.55	31.51	31.48
Stability Derivative	Reference values	Positive Increase (%)			
$C_{n\beta}$ [deg^{-1}]	0.0028	6.31	5.38	3.76	2.49
$C_{L\alpha}$ [deg^{-1}]	0.0825	3.16	3.24	3.29	3.34

Conclusion

In this work, a closely coupled FSI approach was used to investigate the aeroelastic behavior of a transport airplane fitted with winglets. Detailed structural and aerodynamic characteristics could be captured of KC-135, enabling the verification of main effects that arose from the winglet incorporation, verifying how the flexibility of the structures affects the aerodynamic behavior of the wing and the winglet, and to be able to verify how the aerodynamic performance would be affected by changes in the geometry of this winglet.

Besides the validation of the approach adopted here, corroborated by the excellent agreement with wind tunnel and flight test, an outstanding capacity of prediction of the aeroelastic phenomena is available, both qualitatively and quantitatively.

The main utility of modeling these coupled physics is to obtain more accurate metamodels for preliminary studies, calibration of aeroelastic plant models for control purposes, and parametric models to perform multidisciplinary optimization studies. Thus, the objective of utilizing it from the design of morphing winglets is fulfilled.

Copyright statement

References

[1] Bisplingoff R.L., Ashley H., Halfman R.L. *Aeroelasticity*. New York: Dover; 1955.

[2] Fung Y.C. *An introduction to aeroelasticity*. New York: Dover; 1955.

[3] Guruswamy G.P, Byun C. “Fluid-structure interactions using Navier–Stokes flow equations coupled with shell

finite element structures,” AIAA-93-3087, 1993.

[4] Seigel JM, Parthasarathy V, Kingsley GM, Dionne PJ, Harrand VJ, Luker JJ. “Application of a multidisciplinary computing environment (MDICE) for loosely coupled fluid–structural analysis,” AIAA-98-4865, 1998.

[5] Liu F, Sadeghi M, Yang S, Tsai H. “Parallel computation of wing flutter with a coupled Navier–Stokes/CSD method”. AIAA-2003-1347, 2003.

[6] Bird R., Stewart W., Lightfoot N., *Transport phenomena*, 2nd ed., John Wiley & Sons, New York, 2007.

[7] Versteeg HK, Malalasekera. *An introduction to computational fluid dynamics*. Harlow, England: Longman Scientific and Technical; 1995.

[8] ANSYS Inc, Fluent Theory guide, 2015.

[9] P. L. Roe, “Approximate Riemann solvers, parameter vectors and difference schemes,” *Journal of Computational Physics*, 43, 357-372, (1981).

[10] M.S. Liou, C.J. Steffen Jr. “A new flux splitting scheme,” *Journal of Computational Physics*, 107 (1) (1993), pp. 23-39.

[11] P. Batten, M.A. Leschziner, U.C. “GoldbergAverage-state Jacobians and implicit methods for compressible viscous and turbulent flows,” *Journal of Computational Physics*, 137 (1) (1997), pp. 38-78.

[12] ANSYS Inc, Ansys Mechanical APDL, 2015.

[13] Hirt C., Amsden A., Cook J., “An arbitrary Lagrangian-Eulerian computing method for all flow speeds”, *Journal of Computational Physics*, vol. 14, no. 3, pp. 227–253, 1974.

[14] Boffi D., Gastaldi L., “A finite element approach for the immersed boundary method”, *Computers Structures*, vol. 81, pp. 491–501, 2003.

[15] Donea J., Guiliani S., Halleux J.P., “An arbitrary Lagrangian-Eulerian finite element method for transient dynamic fluid-structure interactions”, *Computer Methods in Applied Mechanics and Engineering*, vol. 33, pp. 689–723, 1982.

[16] Deville M.O., Mund E.H., *High-Order Methods for Incompressible Fluid Flow*, Cambridge University Press, 2002.

[17] Farhat C., Degand C., Koobus B., Lesoinne M., "Torsional springs for two-dimensional dynamic unstructured fluid meshes", *Computer Methods in Applied Mechanics and Engineering*, vol. 163, pp. 231–245, 1998.

[18] Hartwich PM, Agrawal S. "Method for perturbing multiblock patched grids in aeroelastic and design optimization applications". AIAA Paper 97-2038, 1997.

[19] National Aeronautics and Aerospace Administration. "KC-135 Winglet Program Review". NASA CP-2211 (1982).

[20] Almojuela, Ben. "The Development of Boeing's 367-80 or charging Into the Jet Age Armed with Only a Slide Rule and Spline,*" Pacific Northwest AIAA Technical Symposium*, Nov. 7, 2009.

[21] The Boeing Commercial Airplane Company. "Summary of the Stability, Control, and Flying Qualities information for All the -135 Series," Seattle, Washington, October 1973.

[22] Niu, M.C.H. "Airframe Structural Design: Practical Design Information and Data on Aircraft Structures," Conmilit Press, 1988.

[23] Sensmeier, M.D. Samaresh, J. A. "A Study of Vehicle Structural Layouts in Post-WWII Aircraft," 45th AIAA/ASME/ASCE/AHS/ASC Structures, Structural Dynamics & Materials Conference, Palm Springs, Califórnia, 19-22 April 2004.

[24] Lloyd, A. - Boeing 707 & AWACS, in detail and scale. Airlife Publishing, 1987.